Aerospace Science and Technology 76 (2018) 155–163

Contents lists available at ScienceDirect

Aerospace Science and Technology

www.elsevier.com/locate/aescte

Shape memory alloy-based mechanism for aeronautical application: Theory, optimization and experiment

Pedro B.C. Leal [a], Marcelo A. Savi [b,*]

[a] Department of Aerospace Engineering, Texas A&M University, College Station 77840, United States
[b] Center for Nonlinear Mechanics, Department of Mechanical Engineering, Universidade Federal do Rio de Janeiro, Rio de Janeiro 21941, Brazil

ARTICLE INFO

Article history:
Received 13 September 2017
Received in revised form 15 December 2017
Accepted 6 February 2018
Available online 13 February 2018

Keywords:
Shape memory alloy
Flap
Optimization
Design

ABSTRACT

Efforts to create efficient and lighter aeronautical structures are defining morphing systems especially those associated with smart materials. In this regard, three simple mechanisms using shape memory alloy (SMA) wires are investigated to generate torque that could be used for flap actuation. The devices consist of an SMA wire biased by a linear spring in the following configurations: concurrent, collinear, and in parallel attached to a pulley. The design of such mechanisms are modeled, optimized, and experimentally verified. The model for the flap consists of two rigid bodies, one fixed and the other rotating, with a single actuator connected to each body. Aerodynamic loading and heat transfer analysis are also considered. The model utilizes the thermomechanical properties for an SMA wire experimentally characterized via improved inverse problem techniques. A multiobjective genetic optimization is implemented to find designs for the three configurations that minimize power consumption and maximize flap deflection magnitude. Overall, as design complexity (i.e., number of degrees of freedom) increases, the power to achieve a certain flap deflection decreases. The maximum deflection for all three mechanisms is sufficient for typical aircraft operations. Finally, numerical results were verified via an experimental apparatus, where similar performance to the model was achieved.

1. Introduction

Aircraft wings are designed to have high performance during cruise, the flight condition that represents the majority of flight time. For other conditions, mechanisms are implemented to modify wing geometry and aerodynamic properties. High-lift devices, such as flaps and slats, are implemented to increment lift during various flight conditions [1]. As an essential aircraft component, flap actuators are compact, have a high fatigue life, and are able to exert high forces. To exceed the limitations of modern actuators built out of traditional materials, the use of smart materials is receiving increased attention. It is the authors' belief that the technical readiness level (TRL) for some of these smart materials is high enough to develop new and realistic aerospace applications. A possible application for flap technology is to substitute pneumatic mechanisms for compact shape memory alloy (SMA) actuators.

Shape memory alloys undergo solid-to-solid phase transformations induced by an appropriate temperature and/or stress [2]. Compared to other actuators, SMA actuators have high actuation stress, high actuation strain, and high energy density [3]. SMA actuator configurations utilizing shape memory effect are classified as either *bias* or *antagonistic* in regards to how the restoring force is applied to the system. A bias configuration consists of one SMA actuator acting against one bias spring. It is characterized as having larger stroke, fast actuation during heating, but slow reset during cooling. An antagonistic configuration consists of a pair of SMA actuators arranged antagonistically. When one actuator is heated, the other remains at room temperature and acts as a stiff spring until it is also heated restoring the initial configuration.

The main challenges for the implementation of SMAs are low energy efficiency and functional fatigue [2], i.e. the loss of actuation stroke over a number of cycles. Accordingly, SMA actuators are suited for applications with low frequency and high force requirements such as flaps. However, the actuators must be designed to reduce energy consumption as demonstrated by Bellini et al. [4] for automotive tumble flaps. Another relevant factor is that the design of high displacement SMA-based mechanisms is not trivial. Although some researchers have obtained significant rigid body displacements utilizing mechanisms with SMA wires [5–7], other researchers have found SMA wires quite limiting [8–10] and even resorted to SMA springs which provide larger stroke in ex-

* Corresponding author.
E-mail address: savi@mecanica.coppe.ufrj.br (M.A. Savi).

https://doi.org/10.1016/j.ast.2018.02.010
1270-9638/

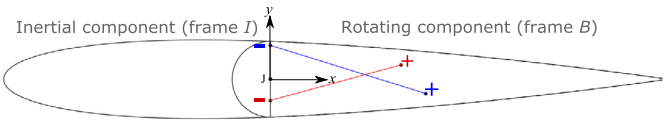

Fig. 1. Design A: schematic of concurrent design (SMA wire in red and elastic spring in blue). (For interpretation of the colors in the figure(s), the reader is referred to the web version of this article.)

change of lower actuation forces [11,12]. Therefore, a complete study of the most common configurations of an SMA wire-based mechanism is beneficial to demonstrate the capabilities not only for aerospace applications, but for any application implementing this mechanism [13].

Previous work from the authors introduced the notion of skin-based camber morphing utilizing SMA actuators for an aircraft wing [14]. Despite the advantages of this technology, manufacturing and switching barriers are an issue. Instead, herein the authors focus on developing a simple SMA-based mechanism that is easy to manufacture and minimizes switching costs. Inspired by prototypes found in the literature for bias configuration [4,5], a bias mechanism consisting of an elastic bias spring and an SMA wire is utilized as driving mechanism for a single-actuated flap. The flap itself acts as a lever for magnifying the displacement of the SMA component which is modeled via the constitutive model by Lagoudas et al. [15], and utilizing properties of the SMA wire obtained following a modified procedure elaborated by Lagoudas et al. [2]. To minimize the effects of small stroke and energy consumption, a multi-objective optimization is undertaken maximizing adiabatic efficiency and flap deflection. The framework implemented can be used to explore several actuation configurations. As such a total of three mechanism designs are considered and compared. One of the mechanisms is experimentally verified.

This work is organized in the following fashion: the mathematical model for the rigid body system is developed in section 2, the experimental characterization of the SMA wires is described in section 3, the numerical/experimental results for the flap system are depicted in section 4, and a summary of the findings is provided in section 5.

2. Mathematical modeling

Morphing structures are becoming important due to adaptive behavior that confers to several applications such as aeronautical systems. As a proof of concept, this paper focuses on the design of a two-dimensional plain flap prototype. For actuation, the mechanism consists of an elastic bias spring and an initially martensitic SMA wire. The following approximations are considered: the model is quasi-static since actuation is slow; the flap components are rigid bodies since deformations and resultant fluid-structure interaction of flap components are negligible; the flap mechanism is simplified to two parts, one fixed and the other free to rotate, connected at joint point J; and each actuator (i.e., SMA wire or linear spring) has one end, point $-$, fixed on the inertial component, while the other end, point $+$, is connected to the rotating component as depicted in Fig. 1. Multiple SMA actuator mechanisms are possible [9,16], but here only three of the most used designs are explored. In decreasing order of complexity, the designs are:

- *Design A – Concurrent*: Inspired by the work by Abreu [9] the design in Fig. 1 is proposed. The end positions of the linear and SMA actuators are independent, and the actuators are concurrent (i.e., each $-$ end can be positioned anywhere on the inertial component and each $+$ end is positioned anywhere on the rotating component). Each actuator is placed on a different parallel plane to the airfoil; hence, the actuators do not intersect each other. Because this design has the most degrees of freedom, eight design variables, a greater design domain is explored.
- *Design B – Collinear*: In this application an SMA actuator is positioned inside of a compression linear spring and both actuators are concentric as depicted in Fig. 2. The two $-$ end points of both actuators are at the same location. The same is true for the $+$ end points. The final design is compact and has only four design variables.
- *Design C – Pulley*: a pulley design is also considered since experimental results by Song et al. [16] showed that it can effectively be used to actuate a flap. The pulley is annexed to the rotating component concentric to point J. When the pulley rotates θ degrees, the flap also deflect θ degrees. Each actuator has the $-$ end point annexed to the inertial component and the $+$ end point attached to a steel wire that connects both actuators. To avoid entanglement of the passive actuator and to thermally isolate the nitinol wire, only the steel wire is in contact with the pulley (see Fig. 3).

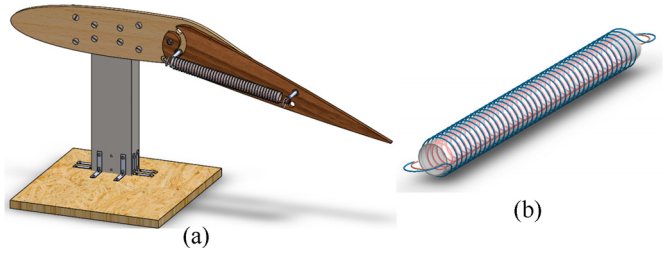

Fig. 2. Design B: collinear actuator design: (a) flap model utilizing collinear actuators; and (b) the actuator itself.

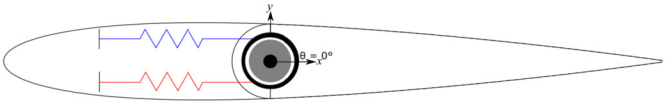

Fig. 3. Design C: actuators connected via a pulley.

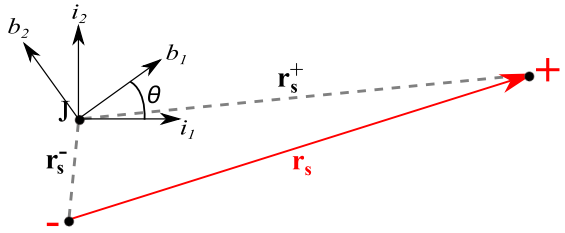

Fig. 4. SMA wire: actuator schematics.

The mathematical modeling for all designs is the same since every concept has two actuators connecting the two rigid bodies, and the deflection angle is torque-driven. In the following sections, the kinematics (section 2.1), governing equation (section 2.2), SMA constitutive model (section 2.3), and thermal performance modeling (section 2.4) are elaborated.

2.1. Kinematics

The spring and the SMA wire have the same geometric and kinematic properties as implied in Fig. 4; hence, the equations derived for this section are valid for both components. If $\mathbf{r}$ is the position vector for an actuator, it can be further decomposed into position vectors $\mathbf{r}^-$ and $\mathbf{r}^+$ (cf. Fig. 4). Since the distance between two points on the same rigid-body is constant, the position vectors $\mathbf{r}^-$ and $\mathbf{r}^+$ are constant in the inertial frame I and body frame

B respectively. If $\mathbf{R}(\theta)$ is a simple 3 rotation tensor around point J for an angle θ, the planar position vector $\mathbf{r}$ is:

$$\mathbf{r} = \mathbf{r}^- + \mathbf{R}(\theta)\mathbf{r}^+ \text{ where, } \mathbf{r}^- = \begin{pmatrix} x^- \\ y^- \\ 0 \end{pmatrix}_I \quad \mathbf{r}^+ = \begin{pmatrix} x^+ \\ y^+ \\ 0 \end{pmatrix}_B . \tag{1}$$

For direct kinematics, the position vector $\mathbf{r}$ is an analytic function of the deflection θ. As for the used sign convention, a clockwise rotation leads to negative angles. For inverse kinematics, a relation based on wire length (equation (2)) is used to estimate the deflection angle θ as a function of actuator strain ϵ and pre-strain ϵ_o.

$$\sqrt{(x^+\cos\theta - y^+\sin\theta - x^-)^2 + (x^+\sin\theta + y^+\cos\theta)^2} - (1+\epsilon-\epsilon_o)||\mathbf{r}_o|| = 0 \tag{2}$$

For a stress-free state, the actuator has length L, i.e., the length of the actuator before coupling to the flap structure. If L is not equal to the magnitude of vector $\mathbf{r}$, the actuator is deformed. If $L > ||\mathbf{r}||$, the actuator is stretched. If $L < ||\mathbf{r}||$, the actuator is compressed. As in the work by Abreu [9], the force $\mathbf{F}$ generated by each actuator is determined by the constitutive model (elaborated in the section 2.3) and has the same direction as position vector $\mathbf{r}$.

2.2. Governing equation

The governing equation is the quasi-static moment equilibrium since the only degree of freedom in the model is the flap angle θ. Considering the torque from all components, the quasi-static moment equilibrium for the system is:

$$\boldsymbol{\tau}_s(\epsilon_s) + \boldsymbol{\tau}_l(\epsilon_s) + \boldsymbol{\tau}_w(\epsilon_s) + \boldsymbol{\tau}_a(\epsilon_s) = 0\,, \tag{3}$$

where each torque component is generated by the SMA actuator ($\boldsymbol{\tau}_s$), the linear spring ($\boldsymbol{\tau}_l$), the weight ($\boldsymbol{\tau}_w$), and the resultant aerodynamic loads ($\boldsymbol{\tau}_a$). As will be seen, it is possible to formulate all the torques as a function of a unique variable, the SMA actuator deformation ϵ_s. The utilized model is temperature driven; as the temperature linearly increases the necessary deformation ϵ_s is calculated to satisfy the quasi-static moment equilibrium. Considering that the deflection θ is calculated as a function of ϵ_s via equation (2), the formulation of each torque is as follows:

- $\boldsymbol{\tau}_s$: the torque provided by the SMA actuator is given by the cross product $\mathbf{r}_s^+ \times \mathbf{F}_s$. The force generated by the SMA actuator is $||\mathbf{F}_s|| = \sigma_s A$, where stress σ_s is obtained from the constitutive model by Lagoudas [15] and A is the cross-section area of the wire.
- $\boldsymbol{\tau}_l$: the torque generated by the linear actuator is given by the cross product $\mathbf{r}_l^+ \times \mathbf{F}_l$. The force $\mathbf{F}_l$ in regards to the strain ϵ_l is linear, e.g. $||\mathbf{F}_l|| = k\epsilon_l L_l$, where k is the spring coefficient and L_l is the original length of the linear spring. The design of the linear spring and calculation of k are undertaken following the procedure from Budynas et al. [17]. The linear spring stiffness coefficient, k, must be high enough to fully detwinne the SMA actuator, hence obtaining maximum stroke.
- $\boldsymbol{\tau}_w$: the weight driven torque is generated by the cross product of the weight vector and the position vector of the center of gravity in regards to the joint point. If W is a scalar that depicts the magnitude of the flap weight, and r_w is the distance from the joint to the center of gravity, the torque $\boldsymbol{\tau}_w$ is:

$$\boldsymbol{\tau}_w = r_w W \cos\theta\ \mathbf{i_3}\,. \tag{4}$$

- $\boldsymbol{\tau}_a$: the resultant aerodynamic torque generated by the pressure gradient along the flap surface is estimated via panel method, which considers a potential flow around the airfoil as a superposition of flow elements that satisfy the Kutta condition. From the definition of the coefficient of pitching aerodynamic moment, $\boldsymbol{\tau}_a$ is:

$$\boldsymbol{\tau}_a = c_{m,J}\,\rho_\infty V_\infty^2 c^2\,\mathbf{i_3}\,. \tag{5}$$

  where $c_{m,J}$ is the two-dimensional moment coefficient at the joint, ρ_∞ is the air density, V_∞ is the aircraft velocity, and c is the chord. The panel method and moment coefficient calculations are implemented via the AeroPy [18] interface to calculate the discrete distribution of pressure coefficients c_p.

To ensure physically meaningful designs, the following kinematic constraints are implemented: the actuators must reside inside the wing structure; and the SMA actuator must not cross the joint point J to avoid zero torque configurations.

2.3. SMA wire constitutive model

The thermomechanical behavior of SMAs can be described by constitutive models that establish a phenomenological description of these alloys. Herein, the model elaborated by Lagoudas et al. [15] is employed and briefly described to introduce the physics behind SMAs and their material properties. The model considers three external state variables (i.e., observable variables): stress σ, total strain ϵ_s, and absolute temperature T. To fully characterize the thermodynamic state of an SMA, the two following internal state variables (i.e., not observable) are also considered: inelastic transformation strain ϵ^t (i.e. caused by detwinning) and martensitic volume fraction ξ. For this paper, temperature is known and defined as a linear function while strain is calculated through the quasi-static moment equilibrium (Eq. (3)). By adding the separate elastic, thermal, and inelastic contributions, the total strain is given as [19]:

$$\epsilon_s = \left[\frac{1}{E_A} + \xi\left(\frac{1}{E_M} - \frac{1}{E_A}\right)\right]\sigma + \alpha_T(T - T_o) + \epsilon^t\,, \tag{6}$$

where E_A and E_M are the Young modulus for austenitic and martensitic phases, respectively; α_T is the thermal expansion coefficient; and T_o is ambient temperature.

Macroscopic phase transformation is induced either by stress or by temperature. Hence, application of stress results in formation or reorientation of martensitic variants. The transformation or detwinning phenomena generates an observable strain ϵ^t [2]. During forward transformation (i.e., austenite to martensite), the inelastic transformation strain rate is dependent on martensitic volume fraction rate and transformation strain. During reverse transformation, it is assumed that the direction and magnitude of transformation strain recovery are governed by the average orientation of the martensite at transformation reversal. Under these assumptions, the evolution of inelastic transformation strain ϵ^t may be expressed by:

$$\dot{\epsilon}^t = \dot{\xi}\begin{cases} \operatorname{sgn}(\sigma)\,H^{cur}(|\sigma|) & \text{for } \dot{\xi} > 0 \\ \epsilon^{t-r}/\xi^r & \text{for } \dot{\xi} < 0 \end{cases}, \tag{7}$$

where H^{cur} is the current transformation strain, ϵ^{t-r} is the transformation strain at transformation reversal, and ξ^r is the martensitic volume fraction at transformation reversal. The magnitude of transformation strain generated during full martensite transformation is captured by the scalar-valued function $H^{cur}(|\sigma|)$. For trained materials, H^{cur} is represented as follows:

$$H^{cur} = \begin{cases} H_{min} & \text{for } |\sigma| \leq \sigma_{crit} \\ H_{min} + \Delta H \left(1 - \exp^{-\kappa(|\sigma| - \sigma_{crit})}\right) & \text{for } |\sigma| > \sigma_{crit} \end{cases} \tag{8}$$

where H_{min}, ΔH, κ and σ_{crit} are material parameters. Other parameters considered in the model are: the transformation temperatures (A_s, A_f, M_s, and M_f) that determine where transformation occurs when no stress is applied, the slope of the transformation surfaces (C_A and C_M), and the hardening parameters (n_1, n_2, n_3, and n_4) that determine the smoothness in the transition between transformation and thermoelastic loading. For more details, see reference [15].

2.4. Thermal performance

The SMA-based mechanism must have similar or improved capabilities in regards to other traditional actuators to make this technology competitive. It needs to generate sufficient torque for significant actuation and also accomplish minimal energy requirements. In this regard, thermal efficiency is the essential point to be considered. Herein, thermal efficiency η is defined as the ratio between generated mechanical work W and input heating load H [20]. As will be seen, work is independent of environment conditions, but the heat load is not. Therefore, the influence of convection must be addressed when defining the system thermal efficiency.

The generated mechanical work W is calculated utilizing the classical definition of work as the inner product of a force vector applied along a path. However, diverging from traditional applications, the stress for an SMA component is not only related to strain but also related to material temperature. Temperature and stress are time dependent and therefore, the total work in its integral form is:

$$W = \int_{t_o}^{t_{final}} \dot{W}(t)dt = A\,L_o \int_{t_o}^{t_{final}} (\epsilon_s \dot{\sigma} + \sigma \dot{\epsilon}_s)\,dt \quad . \tag{9}$$

Temperature is defined as a linear function and the necessary input heating load H to achieve the temperature profile is evaluated. The heating is provided via Joule effect and it must also be sufficient to compensate the energy lost from convection and for the energy used for phase transformation. Thus, power consumption can be defined by the following function of the specific heat/sink term r:

$$H = \int_{t_o}^{t_{final}} \left(\frac{\pi d^2}{4}\right) L_s(t)\,\rho(t)\,r(t)dt \quad , \tag{10}$$

where L_s is the length of the SMA wire, and ρ is the density. L_s is obtained from actuator strain while the product ρr is calculated via the 1-D intrinsic version of the energy conservation model introduced by Tabesh et al. [19]. The model adopts homogeneous temperature distribution and does not consider conduction and end effects, which is acceptable for a thin wire. Consequently, the energy equation for a 1-D wire with heat flux and heat source terms is:

$$\rho c \dot{T} + T\alpha\dot{\sigma} + (-\pi^t + \rho \Delta s_o T)\dot{\xi} = h(T - T_\infty) + \rho r \quad , \tag{11}$$

where c is the specific heat, π^t is the effective thermodynamic driving force for transformation, Δs_o is the reference entropy difference between martensite and austenite, T_∞ is the ambient temperature, and h is heat transfer coefficient due to natural convection. The Nusselt number for natural convection is provided by Kakaç et al. [21]. The left hand side of equation (11) considers thermomechanical coupling effects. Specifically, $T\alpha_T\dot{\sigma}$ represents the thermoelastic heat change present in all material bodies that can be attributed to the change of the volume of a material under elastic load; and the last term is the latent heat related to phase transformation. The right hand side contains terms related to heat entering (Joule heating) or leaving (convection) the system. The thermodynamic driving force π^t and $\rho\Delta s_o$ are functions of the parameters introduced in the previous section. For more information about this formulation, the work by Lagoudas et al. [15] is referred. Since the modeling adopts a temperature-driven model, T and $\dot{T}$ are known. Assuming all other constitutive model terms known, ρr is the only unknown in equation (11). Therefore, the Joule effect term ρr necessary to linearly increase the temperature is calculated via equation (11).

3. Experimental characterization

Nitinol material properties are necessary to design and build the SMA driven flap actuated via an electric current. On the grounds that nitinol components have high sensitivity to manufacturing procedures and heat treatments [2], each wire from different batches are likely to have divergent properties. Therefore, it is necessary to characterize the SMA components in-house. A flexinol wire fabricated by Dynalloy [22] of diameter 0.381 mm is utilized.

Shape memory alloys have thermomechanical coupled properties, e.g., Young's modulus is temperature and stress dependent. Consequently, the characterization process for SMA components is more complex than for other traditional alloys. The characterization of SMA components requires the following three types of experiments: [2]

- **Experiment 1 – DSC test:** Determination of zero-stress transformation temperatures (M_s, M_f, A_s, and A_f) via a differential scanning calorimeter (DSC);
- **Experiment 2 – tensile tests:** Monotonic loading and unloading in martensite ($T < M_s$) and austenite ($T > A_f$) conditions to define Young's moduli for martensite and austenite (E_M and E_A);
- **Experiment 3 – isobaric tests:** Isobaric thermal loading at different non-zero stress levels. Combined with results of the previous two types of experiments, the alloy's transformation slopes (C_M and C_A) and strain deformation properties (H_{min}, ΔH, k, and σ_{crit}) are determined. Transformation temperatures are also calculated via this test.

For experiment 1, a Nietzche DSC 200 F3 is utilized. The testing system Instron 5982 with a thermal chamber, depicted in Fig. 5, is used for experiments 2 and 3. The temperature inside of the camber is controlled by an Eurotherm's 3208 hardware that regulates resistive heating and cooling via liquid nitrogen. A cell load with maximum load capacity of 1 kN and an accuracy of 0.25 N is used since the expected forces are below 100 N.

Overall a two-step procedure is implemented. The first step denominated as *experimental calibration* consists of a traditional set of inverse problems to determine thermomechanical properties (section 3.1). The second step denoted as *numerical calibration* pertains to curve fitting the constitutive model to experimental results (section 3.2) utilizing the preliminary calibrated properties as an initial guess. This extra step is necessary because current constitutive models have complex dependencies that are not fully portrayed in the initial experimental calibration.

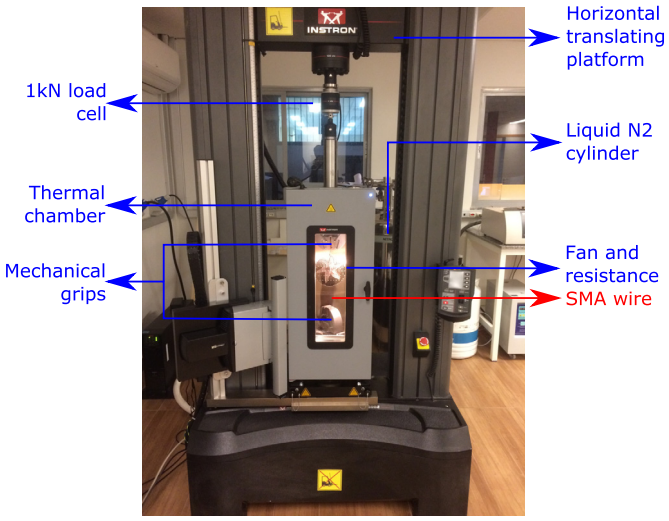

Fig. 5. Instron equipment utilized for thermo-mechanical loadings: testing system and thermal chamber.

3.1. Experimental calibration

In the case of shape memory alloys, it is important to train nitinol wires before the characterization process. *Training* is related to the stabilization of the material under cyclic thermomechanical loads specific to its intended application [2]. The training process consisted of 100 isobaric thermal cycles between 30°C and 140°C, which approximately reproduces the working conditions of the intended flap application. The material is trained for a stress above the intended use, 200 MPa, since overloading a trained material can influence the material's stable response.

Experiment 1 – DSC test A low speed IsoMet saw is utilized to cut an untrained wire sample to reduce residual stress. Two heating/cooling cycles were undertaken with the DSC equipment from −40°C upto 140°C. Transformation temperatures are estimated via Nietzsche's tangent method furnishing the values $M_s = 49.9°C$, $M_f = 31.6°C$, $A_s = 74.8°C$, and $A_f = 79.8°C$.

Experiment 2 – tensile tests Two tensile tests are undertaken utilizing the Instron equipment. The first is a rupture test for an untrained SMA wire at room temperature; thus the wire is in the martensite phase according to DSC results. The ultimate stress is 1248 MPa. For stress below 200 MPa, the material behaves in a linear fashion and a martensitic Young modulus E_M of 91.01 GPa is obtained via linear regression. The second test is a 200 MPa cyclic loading of a trained SMA wire at 140°C. From the results in experiment 1, we have that the wire is purely in the austenite phase. Utilizing linear regression once again for stresses below 200 MPa, the initial estimate for austenite Young modulus E_A is 44.93 GPa.

Experiment 3 – isobaric tests Results for five isobaric tests at constant stresses 50, 100, 150, 172, and 200 Mpa are given in Fig. 6a. The purpose of the isobaric thermal loading tests is to develop the material's phase diagram and maximum recoverable transformation strain H^{cur} curve (equation (8)). The obtained data from the experiments is processed and utilized in inverse problems to calculate the desired properties. A differential evolution algorithm is implemented to minimize the root mean squared error between the experimental data and the numerical model.

It was experimentally verified that there was a stress variation when heating the wire initially free of stress and with an imposed

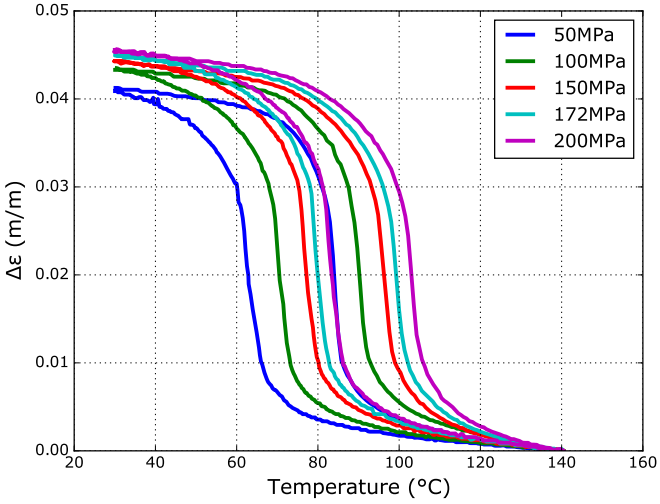

(a) Influence of stress over hysteresis.

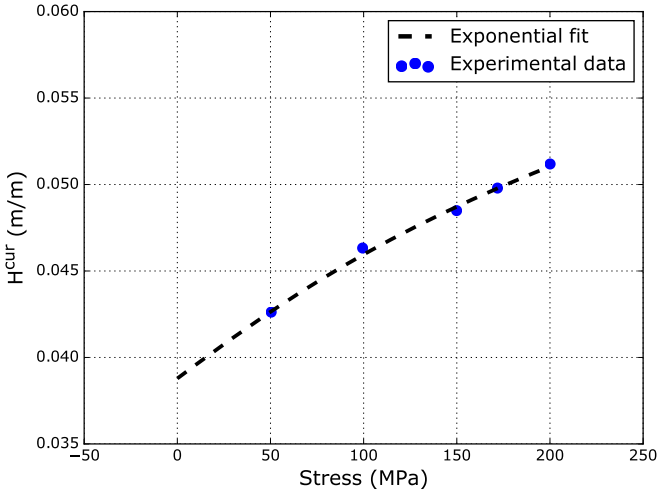

(b) Maximum recoverable transformation strain.

Fig. 6. Data from isobaric temperature driven experiments related to transformation strain.

constant length. If actuator strain is constant and thermal expansion is negligible, only a variation in transformation strain would be responsible for the stress variation (equation (6)). Therefore, this indicates that at $\sigma = 0$, the maximum recoverable transformation strain is not zero, and the critical stress where recoverable transformation strain is generated is $\sigma_{crit} = 0$. The result from the differential evolution optimization with a population of 200 and 100 generations is depicted in Fig. 6b, and the fitted parameters are $H_{min} = 0.03878$, $H_{max} = 0.06272$, and $\kappa = 0.00359$ MPa^{-1}. Fig. 6b shows that the calibrated H^{cur} function accurately portrays material behavior.

The data from the isobaric thermal loading tests is also used for calculating transformation temperatures for non-zero stresses. Lagoudas [2] conventionally utilizes the tangent method to find transformation temperatures. The original tangent method consists of three lines drawn tangent to different points of a strain versus temperature plot; the intersection of these lines indicate the transformation temperatures similar to Fig. 7a. However, for the obtained experimental data, the tangent method is imprecise and highly sensitive. Instead, an alternative method is utilized to automate the process and to improve accuracy. Following this concept, a discrete function composed of three linear domains is proposed

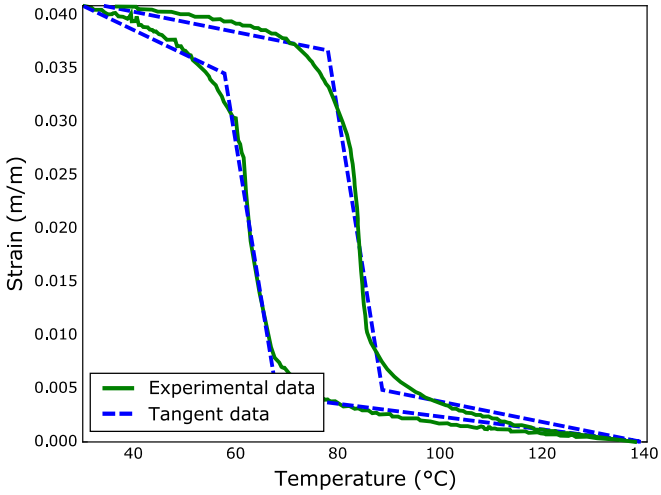

(a) Isobaric thermal loadings and modified tangent method for 50 MPa.

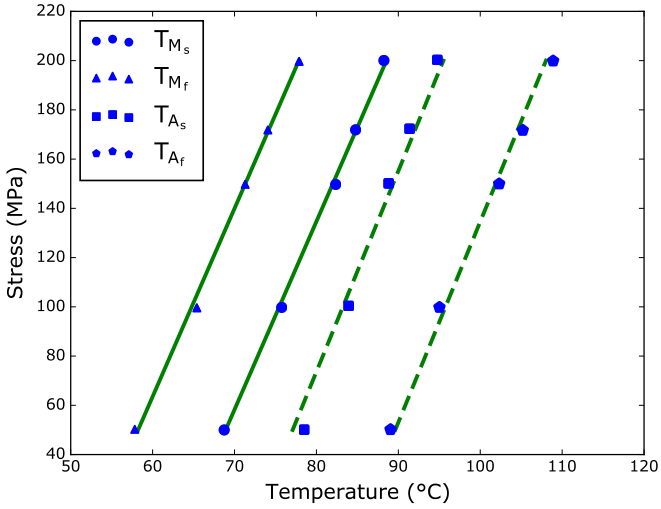

(b) Fitted phase diagram based on tangent method results.

Fig. 7. Data from isobaric temperature driven experiments related to transformation temperatures.

to curve fit experimental data independently for heating and another for cooling. The proposed function is summarized as:

$$\epsilon^{tangent}(T) = \begin{cases} \frac{\epsilon_2-\epsilon_1}{T_2-T_1}(T-T_1)+\epsilon_1 & \text{for} \quad T \leq T_2 \\ \frac{\epsilon_3-\epsilon_2}{T_3-T_2}(T-T_2)+\epsilon_2 & \text{for} \quad T_2 \leq T \leq T_3 \\ \frac{\epsilon_4-\epsilon_3}{T_4-T_3}(T-T_4)+\epsilon_3 & \text{for} \quad T \geq T_3 \end{cases}, \tag{12}$$

where T_1 is the minimum temperature, T_4 is the maximum temperature, and T_2 and T_3 are in-between transformation temperatures. When heating T_2 is A_s, and T_3 is A_f, while for cooling T_2 is M_f, and T_3 is M_s. For all problems $T_1 = 30°C$ and $T_4 = 140°C$, while T_2 and T_3 are adjusted via the optimization algorithm. All fitted strains $\{\epsilon_1, \epsilon_2, \epsilon_3, \epsilon_4\}$ are calculated, but do not represent meaningful material properties.

A summary of all calculated transformation temperatures according to stress are given by the phase diagram in Fig. 7b, where the fitted transformation surfaces are also depicted. Since the transformation surface slopes C_M and C_A are equal for start and finish surfaces, a simple linear regression did not suffice; hence an optimization problem was considered where the root mean

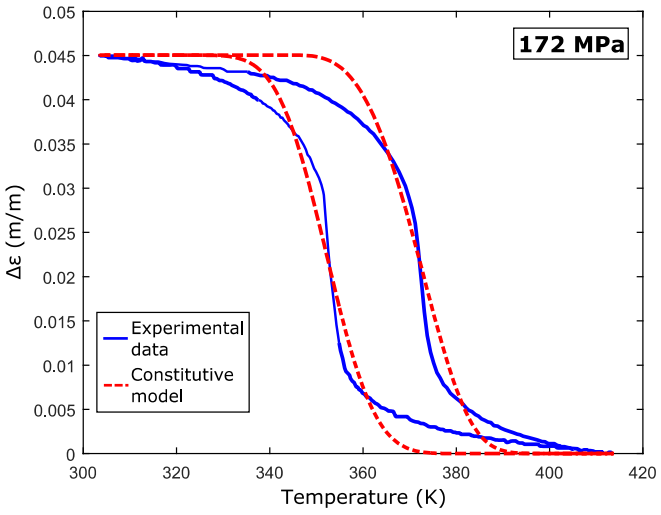

Fig. 8. Verification of fitted parameters for experimental data at a constant stress of 172 MPa.

squared error for both surfaces are simultaneously minimized via differential evolution. The values obtained are $C_A = 7.64$ MPa/K and $C_M = 8.15$ MPa/K. As a result from this last calibration, the transformation temperatures at zero stress are also calculated as $M_s = 62.38°C$, $M_f = 51.69°C$, $A_s = 70.96°C$, and $A_f = 83.49°C$. The difference in temperature measurements can be either be associated with the inherent error from the calculations or from the influence that training has over transformation temperatures.

3.2. Numerical calibration

Previous section utilized experimental data to find traditional shape memory alloy parameters in three different inverse problems. However, in recent models [15,19] transformation surfaces are not only dependent of transformation temperatures and slopes, but also dependent of Young moduli, maximum recoverable transformation strain H^{cur}, and hardening parameters (n_1, n_2, n_3, and n_4) [15]. To accurately portray the behavior of SMA wires, a final calibration step is undertaken where all the material parameters experimentally calibrated are utilized as an initial guess for the constitutive model that will be curve fitted to the experimental data from isobaric tests for stresses 50, 100, 150 and 200 MPa via a Newton–Raphson optimizer (cf. Fig. 6). Compared to the experimental data in Fig. 8, the fitted constitutive model response portrays the resultant strain and resembles the experimental result; this is considered as sufficient to verify the numerically calibrated properties.

All of the calculated thermomechanical properties including the hardening parameters are provided in Table 1. After the numerical calibration, all thermomechanical properties except for the transformation temperatures did not vary significantly; hence, the initially experimentally calibrated properties were close to accurately depicting the material's behavior. The transformation temperatures significantly changed because of smooth hardening [15].

4. Flap mechanism analysis

A flap is a high-lift device utilized to modify an aircraft outer mold line to increase lift. In modern aeronautics, flaps are essential components, being mostly utilized for take-off and landing. A flap actuator must be reliable and generate high torque. While efficiency is not a requirement, it is a desired trait. This section discusses flap mechanism morphing considering minimum energy cost. The mathematical modeling introduced in section 2 is herein

Table 1
Calibrated SMA wire properties.

Property	Value	Property	Value
ρ (kg/m^3) [22]	6450	σ_{ultimate} (MPa)	1268.1
E_M (GPa)	88.88	E_A (GPa)	37.43
ν_M [22]	0.33	ν_A [22]	0.33
α_M (10^{-6}/K) [22]	11.0	α_A (10^{-6}/K) [22]	6.6
c (J/(kg K)) [23]	320		
C_M (MPa/K)	7.12	C_A (MPa/K)	8.04
M_s (°C)	62.38	A_s (°C)	70.96
M_f (°C)	51.69	A_f (°C)	83.49
$H_{\min}$ (m/m)	0.0387	ΔH (m/m)	0.0163
κ (1/MPa)	0.00597	σ_{crit} (MPa)	0
n_1	0.1752	n_2	0.1789
n_3	0.1497	n_4	0.2935

Table 2
Constant parameters.

Variable	Value	Variable	Value
Angle of attack	0	Altitude	3000 m
Chord	1 m	V_∞	10 m/s
Joint x-coordinate	0.75 m	Joint y-coordinate	0 m
Flap CG	0.85 m	Pre-tension	100 MPa
T_o	30°C	T_{max}	140°C
W	0.513 N	r_W	0.1 m
Spring index	10	Safety factor	5

implemented for the three proposed designs (A, B, and C) of the bias SMA mechanism utilizing the SMA wire properties determined in section 3. Numerical procedure adopted to deal with mathematical model is proposed in section 4.1. Mathematical models for the three designs are optimized in a multi-objective problem (section 4.2). Another optimization is undertaken to obtain the maximum deflection for each design and evaluate the influence of convection (section 4.3). Finally an experimental apparatus of an SMA driven flap is fabricated to verify the mathematical model (section 4.4).

4.1. Numerical procedure

A quasi-static temperature driven simulation is performed. For each temperature, governing equation solution is calculated. SMA wires constitutive modeling is accomplished via a MATLAB code while the aerodynamic moment τ_a is calculated at each iteration via the AeroPy interface [18]. A fixed-point iteration method is implemented until convergence is obtained for each temperature increment.

The optimal design for the problem proposed is not trivial. The positioning of the actuators influences the total stroke, the length of the actuators, the moment arm, and maximum actuation temperature without violating kinematic constraints. Therefore, an optimization algorithm is necessary. In order to minimize the number of design variables, certain values such as the spring index and safety factor considered for the spring designs, are held constant (Table 2). The design variable vector $\mathbf{x}$ is composed only of the coordinates of the actuator end points. The lower and upper limits of the design variables, $\mathbf{x}^{lower}$ and $\mathbf{x}^{upper}$, are the lower and upper airfoil surfaces. Other non-defined aerodynamic properties, such as air density, are calculated either via Sutherland's Law [24] or by interpolating known air property values.

4.2. Multiobjective design comparison

High power requirements are undesirable on the grounds that it makes this technology less competitive when compared to other traditional actuators. Therefore, it is important to reduce power consumption without losing actuation capability. Accordingly, a multi-objective optimization is implemented with deflection θ and power consumption H as objective functions. A genetic algorithm [25] is utilized to find the set of optimal solutions known as a Pareto frontier (50 generations and population size of 40). An optimal solution in a multi-objective optimization context is a solution where there exists no other feasible solution that improves the value of at least one objective function without deteriorating any other objective. As such, the optimization problem is given by:

$$\begin{aligned} &\min_{\mathbf{x}} \quad \theta(\mathbf{x}) \text{ and } H(\mathbf{x}) \\ &\text{subject to } \mathbf{x}^{lower} \leq \mathbf{x} \leq \mathbf{x}^{upper} \end{aligned} . \tag{13}$$

Utilizing the quasi-static simulation previously developed and taking into consideration the effects of natural convection, the multi-objective optimization is implemented for all designs to obtain the Pareto frontier in Fig. 9. In regards to power consumption per flap deflection, design A (concurrent) has the best profile for all possible flap deflections. While design B (collinear) consumes a similar amount of power as design A for small deflections, its efficiency decreases for greater deflections. As for design C (pulley), it is less efficient than the other two for any flap deflection. As usual in multi-objective optimization, there is not a unique solution to the problem and a posteriori decision is necessary to choose the desired solution. Therefore, the Pareto frontier enables an engineer to select a flap design based on the amount of power or deflection necessary. For example, if a power source of five joules is utilized, a simple mechanism utilizing a pulley can guarantee a $-12°$ rotation, but with an increasing order of complexity, other designs can be used to obtain $-15°$ and $-20°$ rotations.

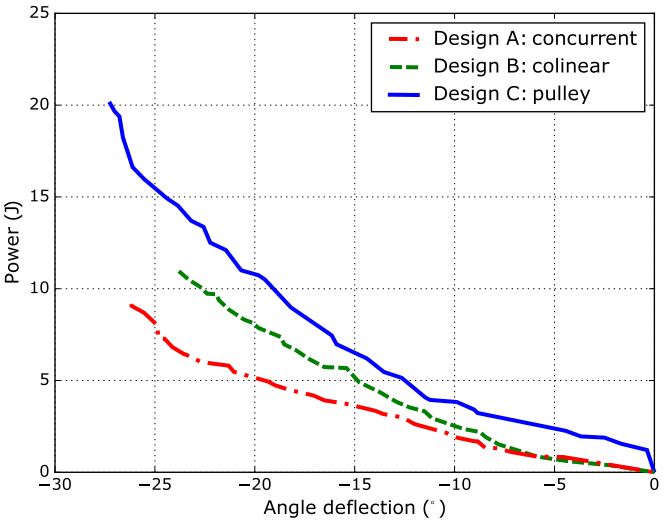

Fig. 9. Comparison of Pareto frontiers (i.e. optimal solutions) for designs A, B, and C.

4.3. Maximum deflection design comparison

To further demonstrate the capability of obtaining large flap displacements with the proposed SMA-driven mechanism, a single objective optimization is implemented for each design to maximize flap deflection magnitude regardless of energy consumption. As in the previous optimization, a differential evolution algorithm is utilized. A summary of the single-optimization results is presented in Table 3. Design A, depicted in Fig. 10, is able to obtain the greatest flap deflections with the least amount of SMA wire and with low stiffness springs. Furthermore, the moment arm of the linear actuator is also reduced to the minimum possible when at austenite; further facilitating greater deflections by reason of the smaller

Table 3
Comparison between maximum deflection solutions for the three designs.

Outputs	Design A	Design B	Design C
Max. deflection (°)	−38.9	−27.7	−27.4
k (N/m)	56.36	482.95	395.13
SMA length (m)	0.363	0.421	0.600

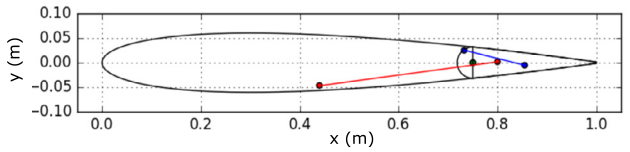

(a) Before heating.

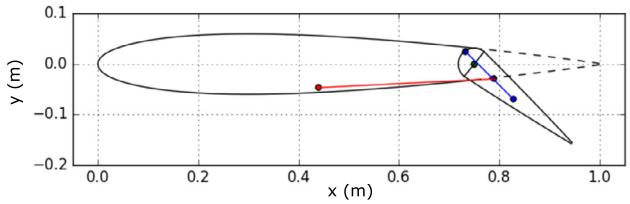

(b) After heating.

Fig. 10. Schematics of optimized design A airfoil for maximum deflection configuration with: (a) no actuation and (b) full actuation. SMA actuator is depicted in red and passive spring in blue.

restoring torque generated by the linear actuator. This design treat is noticeable in all optimized solutions for designs A and B.

The optimization results for design C entices that high radius and SMA length are desirable for obtaining greater deflections. The former is expected since torque is linearly proportional to the radius. The latter takes place because longer wires result in greater wire translations, thus greater pulley rotations. Since SMA wire for design C is longer than for designs A and B, more heat is necessary to obtain similar flap deflection as stated in Fig. 9. Therefore, the optimal solution for design C has low energetic efficiency. Nevertheless, a mechanism with optimal performance for design C is easier to determine as long as a high radius and a long SMA wire are used.

Utilizing the methodology explained in section 2.4, the influence of convection over required heat and generated work are calculated for the maximum deflection configuration for design A. The total adiabatic heat is 15.2 Joules and the output work is 1.36 Joules that results in a thermal efficiency of 8.9 % percent. The low efficiency is in accordance to experimental results by Jackson et al. [20]. Considering that the work generated is independent of heat flux, the influence of convection coefficient h and actuation period, i.e. time period where an electric voltage is applied, is considered and depicted in Fig. 11. A greater convection coefficient and a longer actuation period lead to increased convection heat loses; hence, a decrease in efficiency.

4.4. Experimental verification of design A

An experimental apparatus was built to verify the mathematical model utilized. The built prototype is depicted in Fig. 12a. The model of half of an airfoil consists of two medium density fiberboard (MDF) components, where the length of the joint to the trailing edge is 25% of the chord. A bearing is utilized at the joint to reduce friction in junction with a set of bolts, washers, and nuts connecting the MDF components. Furthermore, a spring is attached by two hooks at each flap component. The utilized spring has a wire diameter of $d = 0.75$ mm, spring diameter $D = 7.25$ mm, zero stress length $L_o = 58.80$ mm, and total number of coils $N_t = 67$.

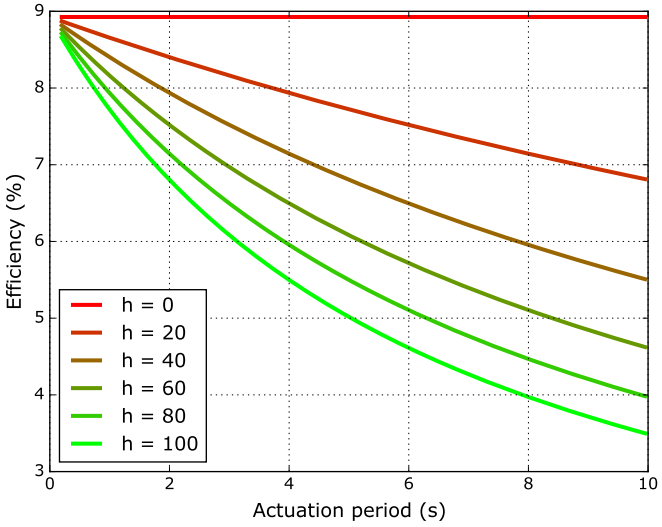

Fig. 11. Efficiency for different actuation duration and convection coefficients for design A.

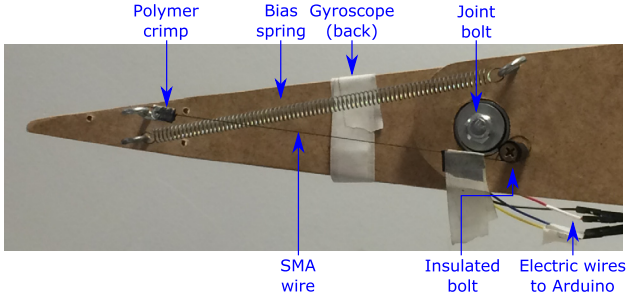

(a) Photo of experimental flap apparatus.

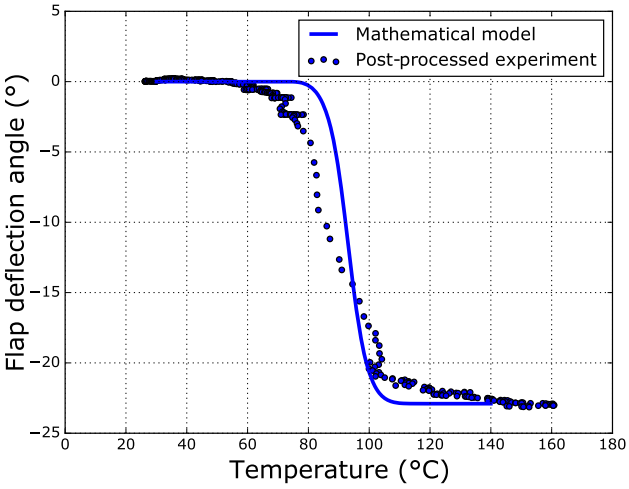

(b) Experimental results.

Fig. 12. Experimental verification of flap deflection model.

According to Budynas et al. [17], the spring stiffness k is estimated as 127.33 N/m. A trained SMA wire is also attached to the two components, with one end attached to a hook via a polymer crimp and the other end attached to an insulated bolt. The bolt is also utilized to pretension the SMA wire. The wire has a diameter of 0.381 mm and is 4.2 cm long. Finally a micro-controller Arduino Mega 2560 is utilized to vary voltage and collect data from a gyroscope sensor ACS712 that is also attached to the flap. When comparing the experimental results to the numerically calibrated model in Fig. 12b there is a strong agreement between results.

5. Conclusions

The design of SMA actuated adaptive flap is investigated. A quasi-static fluid-structure model of an flap driven by a mechanism consisting of an SMA wire and a bias linear spring is proposed and developed considering three different actuator configurations: concurrent, collinear, and in parallel attached to a pulley. SMA actuator is a nitinol wire that is thermomechanically characterized utilizing inverse problem and optimization algorithms. Besides, a proper constitutive model is employed for its thermomechanical description. The final calibrated constitutive model is obtained via a modified tangent method and it properly reproduces experimental data. Taking into consideration the calibrated SMA properties as well as all of the geometric and physical restrictions, a multi-objective optimization is implemented to obtain a Pareto frontier that minimizes energy consumption while maximizing the flap deflection for each design. All designs are able to achieve significant deflections, but the concurrent configuration achieves higher flap deflections (up to 38°) with an energy efficiency (work over input heat) of 8.9%. Overall, concurrent actuators require less energy than other configurations. However, for small deflections, concurrent and collinear configurations have similar power costs. A pulley based configuration has worst performance, but it is the easiest configuration to build for large flap deflections. As long as the SMA wire and the pulley radius are large, the obtained deflection is significant. An experimental apparatus of the SMA-driven flap was developed consisting of an SMA wire and a bias spring in a concurrent configuration. Experimental measurements are in close agreement with numerical results.

Conflict of interest statement

There is no conflict of interest.

Acknowledgements

The author would also like to acknowledge the support of the Brazilian Research Agencies CNPq, CAPES and FAPERJ. The Air Force Office of Scientific Research (AFOSR, grant number FA9550-16-0381) is also acknowledged. The authors are grateful to Embraer who supported part of this study.

References

[1] J.D. Anderson, Fundamentals of Aerodynamics, 5th edition, Anderson Series, McGraw-Hill, New York, 2011.
[2] D. Lagoudas, Shape Memory Alloys: Modeling and Engineering Applications, 1st edition, Springer, New York, 2008.
[3] D.J. Hartl, D.C. Lagoudas, Aerospace applications of shape memory alloys, Proc. Inst. Mech. Eng., G J. Aerosp. Eng. 221 (4) (2007) 535–552.
[4] A. Bellini, M. Colli, E. Dragoni, Mechatronic design of a shape memory alloy actuator for automotive tumble flaps: a case study, IEEE Trans. Ind. Electron. 56 (7) (2009) 2644–2656.
[5] M.H. Elahinia, H. Ashrafiuon, Nonlinear control of a shape memory alloy actuated manipulator, J. Vib. Acoust. 124 (4) (2002) 566.
[6] M. Senthilkumar, Analysis of SMA actuated plain flap wing, J. Eng. Sci. Technol. Rev. 5 (1) (2012) 39–43.
[7] J.N. Kudva, Overview of the DARPA smart wing project, J. Intell. Mater. Syst. Struct. 15 (4) (2004) 261–267.
[8] G. Song, B. Kelly, B.N. Agrawal, Active position control of a shape memory alloy wire actuated composite beam, Smart Mater. Struct. 9 (5) (2000) 711.
[9] G.L. Abreu, Controle nebuloso aplicado em asas adaptativas utilizando ligas de memória de forma, Mechanical Engineering Master Thesis, Faculdade de Engenharia, Universidade Estadual Paulista – UNESP, 2012.
[10] M. Moallem, V.A. Tabrizi, Tracking control of an antagonistic shape memory alloy actuator pair, IEEE Trans. Control Syst. Technol. 17 (1) (2009) 184–190.
[11] S. Enemark, M.A. Savi, I.F. Santos, Nonlinear dynamics of a pseudoelastic shape memory alloy system – theory and experiment, Smart Mater. Struct. 23 (8) (2014).
[12] R.A.A. Aguiar, M.A. Savi, P. Pacheco, Experimental and numerical investigations of shape memory alloy helical springs, Smart Mater. Struct. 19 (2) (2010) 025008.
[13] P. Monteiro Jr, L. Silva Monteiro, M.A. Savi, T. Netto, P. Pacheco, T. de Paiva, A comparative analysis of different shape memory alloy actuator configurations, J. Intell. Mater. Syst. Struct. 28 (11) (2017) 1415–1427.
[14] P.B. Leal, M.A. Savi, D.J. Hartl, Aero-structural optimization of shape memory alloy-based wing morphing via a class/shape transformation approach, Proc. Inst. Mech. Eng., G J. Aerosp. Eng. (2017) 095441001771619.
[15] D. Lagoudas, D. Hartl, Y. Chemisky, L. Machado, P. Popov, Constitutive model for the numerical analysis of phase transformation in polycrystalline shape memory alloys, Int. J. Plast. 32–33 (2012) 155–183.
[16] G. Song, N. Ma, Robust control of a shape memory alloy wire actuated flap, Smart Mater. Struct. 16 (6) (2007) N51–N57.
[17] R.G. Budynas, J.K. Nisbett, J.E. Shigley, Shigley's Mechanical Engineering Design, tenth edition, Mcgraw-Hill Series in Mechanical Engineering, McGraw-Hill Education, New York, NY, 2015.
[18] P.B.C. Leal, AeroPy: An easy to use aerodynamics tool, 2016.
[19] M. Tabesh, B. Lester, D. Hartl, D. Lagoudas, Influence of the latent heat of transformation and thermomechanical coupling on the performance of shape memory alloy actuators, in: ASME 2012 Conference on Smart Materials, Adaptive Structures and Intelligent Systems, American Society of Mechanical Engineers, 2012, pp. 237–248.
[20] C.M. Jackson, H.J. Wagner, R.J. Wasilewski, The Alloy with a Memory, 55-Nitinol: Its Physical Metallurgy, Properties, and Applications, 1972.
[21] S. Kakaç, R. Shah, W. Aung, Handbook of Single-Phase Convective Heat Transfer, 1987.
[22] Dynalloy, Technical Characteristics of Flexinol Actuator Wires F1140rev I.2 – TCF1140.pdf, 2014.
[23] R. Velázquez, E.E. Pissaloux, Modelling and temperature control of shape memory alloys with fast electrical heating, Int. J. Mech. Control 13 (2012) 1–8.
[24] M. Drela, Flight Vehicle Aerodynamics, The MIT Press, 2014.
[25] K. Deb, A. Pratap, S. Agarwal, T. Meyarivan, A fast and elitist multiobjective genetic algorithm: NSGA-II, IEEE Trans. Evol. Comput. 6 (2) (2002) 182–197.